ADVANCED FUNCTIONAL MATERIALS
www.afm-journal.de

Materials Views
www.MaterialsViews.com

Carbon-Based Yolk–Shell Materials for Fuel Cell Applications

*Carolina Galeano, Claudio Baldizzone, Hans Bongard, Bernd Spliethoff, Claudia Weidenthaler, Josef C. Meier, Karl J. J. Mayrhofer, and Ferdi Schüth**

The synthesis of yolk–shell catalysts, consisting of platinum or gold–platinum cores and graphitic carbon shells, and their electrocatalytic stabilities are described. Different encapsulation pathways for the metal nanoparticles are explored and optimized. Electrochemical studies of the optimized AuPt, @C catalyst revealed a high stability of the encapsulated metal particles. However, in order to reach full activity, several thousand potential cycles are required. After the electrochemical surface area is fully developed, the catalysts show exceptionally high stability, with almost no degradation over approximately 30 000 potential cycles between 0.4 and 1.4 V_{RHE}.

1. Introduction

Core–shell and yolk–shell materials are interesting systems for a variety of applications. Especially in catalysis, such systems can offer properties which are a combination of the advantageous features of the constituents. One application field of core–shell and yolk–shell materials is heterogeneous catalysis. In 2006, we have reported the stabilization of gold colloidal catalysts against sintering during high temperature CO oxidation by encapsulation in zirconia hollow shells.[1] Later on, Joo et al.[2] reported the synthesis of Pt@mesoporous-SiO_2,[1] consisting of Pt nanoparticles of ≈15 nm encapsulated in a mesoporous silica shell, and its uses in high temperature gas phase reactions. Furthermore, core@shell materials with magnetic cores like Fe,[3,4] Co,[5] or Ni[6] are used in heterogeneous catalysis as magnetically recoverable solid catalysts, where usually the catalytically active phase corresponds to the shell material and the core provides the magnetic properties to the system.[4]

Yolk–shell materials, also known as rattle-type particles, are special extensions of core@shell systems. They are composed of a solid particle as core, an interstitial free space between core and shell, and the (in most cases porous) shell. Yolk–shell particles have mostly been synthesized by templating strategies using core–shell materials as building blocks. Their synthesis often relies on the concepts initially developed by Liz-Marzán and colleagues.[7] For instance, Park et al.[6] described the synthesis of Ni@SiO_2 by coating pre-formed Ni particles with a mesoporous silica shell by modification of the Stöber process. The initial Ni@SiO_2 core@shell material was transformed to yolk–shell materials by partially leaching the Ni core. These materials were used as methane steam reforming catalysts with high thermal stability. Furthermore, the same synthesis strategy was extended to Fe@SiO_2 and Co@SiO_2 core@shell structures.

Basically, there are two general approaches to produce yolk–shell structures. The first one is based on a bottom-up approach, in which the system is fabricated in an inside to outside order. A first pathway involves the preparation of the core followed by the consecutive coating with a spacer layer, and finally the outer layer of the targeted shell material. The spacer layer is finally removed via selective dissolution or calcination. As examples, Au, @polymer,[8] Au, @SiO_2,[9] Au, @C,[8,9] Pt, @C,[10,11] and Rh, @C[12] have been obtained using bottom-up strategies and silica as spacer layer. Additionally, Au, @Fe_3O_4[13] has been synthesized using as spacer layer organic molecules like oleylamine/oleic acid. A second pathway involves the creation of the inner void by partial dissolution of the central shell material by Ostwald ripening.[14,15] In contrast, a third pathway relies on the creation of the inner void by partial dissolution of the core material of the initial core–shell system.[6,16,17]

The alternative to the bottom-up approaches described above is a top-down approach, also called pre-shell post-core method. Following this method, first hollow spheres are generated by hard templating or soft templating strategies. Subsequently, the core of interest can be included into the shell via permeation of the precursor and subsequent chemical treatment, for instance chemical reduction[18,19] or metal displacement reactions.[20] Hah et al.[20] reported the preparation of Cu core rattle-type silica particles by a pre-shell/post-core synthetic route. In the same work, the exchange of the Cu metal cores inside silica shells for Ag cores was achieved by a metal displacement reaction.

Yolk–shell materials have not only attracted interest due to their unique structure, but also because they provide interesting functionality. For instance, sinter-stable materials can be based on such systems. The encapsulated metal nanoparticle is successfully hindered by the shell to migrate out and further sinter with other metal nanoparticles. In addition to the

C. Galeano, H. Bongard, B. Spliethoff,
Dr. C. Weidenthaler, Prof. F. Schüth
MPI für Kohlenforschung
Kaiser-Wilhelm-Platz 1, 45470, Mülheim, Germany
E-mail: schueth@kofo.mpg.de
C. Baldizzone, J. C. Meier, Dr. K. J. J. Mayrhofer
MPI für Eisenforschung
Max-Planck-Straße 1, 40237, Düsseldorf, Germany

DOI: 10.1002/adfm.201302239

© 2013 WILEY-VCH Verlag GmbH & Co. KGaA, Weinheim

stability against sintering, yolk–shell materials often provide rather monodisperse and narrow particle size distributions. This makes these materials highly suitable as model catalysts, which allow the study of general problems in heterogeneous catalysis, such as particle size dependence of catalytic activity or metal-support interactions. Representative examples of yolk–shell systems designed in our group for CO oxidation are Au nanoparticles encapsulated in metal oxide shells, like zirconia (Au, @ZrO_2),[1,21–23] and titania (Au, @TiO_2).[24] Core@shell materials like Au@SnO_2[25] and Pt@*m*-SiO_2[2] have also been reported as CO oxidation catalysts.

Encapsulation could also improve the stability of fuel cell catalysts, provided that a conducting shell, such as carbon, could be created. There are five major deactivation pathways of fuel cell cathode catalysts,[26–29] coalescence and detachment of metal nanoparticles from the support, platinum dissolution, Ostwald ripening, and carbon support corrosion. Encapsulation of the active phase in a carbon shell could slow down or even prevent most of these pathways. Agglomeration of particles located in different spheres and detachment of particles is completely suppressed by encapsulation. Since the cores are relatively monodisperse in yolk–shell particles (if colloidal synthesis is used for the creation of the cores) the driving force for Ostwald-ripening is very low. Dissolution could also be slowed down, because the concentration increases relatively quickly in the shell, reducing the driving force for further dissolution. Furthermore, if graphitic carbon shells were used, the graphitization could also improve carbon corrosion resistance.

The requirements for such core–shell systems for applications in electrocatalysis are as follows: 1) the shell has to have sufficiently high electron conductivity; 2) the shell has to be sufficiently porous in order to allow the transport of electrolyte and gaseous reactants to the encapsulated metal nanoparticle; 3) the metal loading has to be as high as possible to achieve significant reaction rates. Commercial fuel cell catalysts have typical noble metal loadings which can reach 50 wt%, or even exceed this value. Therefore, the shell diameter and the size of the metal nanoparticles have to be modifiable in order to adjust the metal loading.

In order to explore the perspectives of such systems, we have relied on the synthetic pathways explored by us for the preparation of sinter-stable catalysts, but expanded the synthesis to platinum and bimetallic platinum-based core particles, encapsulated in graphitized carbon shells. The goal of the study was the exploration of synthetic protocols for electroactive yolk–shell catalysts, and tests of their performance as cathode catalysts for low temperature fuel cells. An alternative approach for stabilization of nanoparticles, introduced by classical impregnation followed by high temperature treatment, in the defined pores of hollow graphitic shells has been reported by us recently.[30]

2. Synthesis of Yolk–Shell Materials

2.1. Optimization of the Carbon Shell Material

The overall synthetic approach is based on the one developed for 15 nm Au, @C published recently by us.[31] Principally,

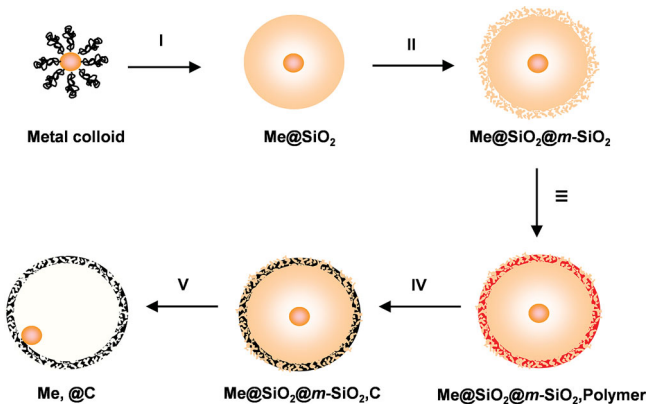

Figure 1. Strategy for the preparation of encapsulated metal nanoparticles in porous carbon shells by nanocasting using the Me@SiO_2@*m*-SiO_2 as exotemplate.

the synthesis follows the pathway sketched in **Figure 1**. A pre-synthesized, ligand-stabilized metal nanoparticle (Me) is coated with a dense silica shell, following a modified Stöber protocol described by Graf et al.[32] The subsequent layer consists of porous silica which is synthesized onto the solid silica sphere by the process described by Büchel et al.[33] This step consists in the hydrolysis/co-condensation reactions of a mixture of tetraethyl orthosilicate (TEOS) and an *n*-octadecyltrimethoxysilane (OTMS), at the surface of the pre-synthesized Me@SiO_2. The OTMS contains an aliphatic substituent group, which during the polycondensation reactions occupies a large space in the silica shell. After calcination at 550 °C in air, the aliphatic groups are burnt, generating the pore system (step II). This core@shell material Me@SiO_2@*m*-@SiO_2, is used as exotemplate for the nanocasting of the carbon shell. During the nanocasting process, polymer precursors (monomers and catalyst/initiator) are selectively infiltrated in the mesopores of the exotemplate. The infiltration of the monomers is carried out via the incipient wetness method, in a way that no precursor material remains outside of the shell, otherwise the core@shell particles (Me@SiO_2@*m*-SiO_2,Polymer) would agglomerate. Afterwards, the monomers are polymerized in the confined space of the mesopores, producing the polymer composite (step III). The polymer is then carbonized at high temperatures under either inert atmosphere or vacuum (step IV). The carbon composite contains the carbon replica which is obtained by leaching of the silica exotemplate with HF or NaOH (step V). During the carbon nanocasting process, the graphitization of the carbon shell can be assisted by transition metal salts. In the next sections, the optimization of the synthesis of the exotemplate and the nanocasting process will be addressed in detail.

In our previous publication, poly(furfurylalcohol) (PFA) had been used as the carbon precursor. In order to explore the scope of the method and optimize the graphitization for use as fuel cell catalysts, also other polymer precursors were used for the nanocasting of the shell, i.e., poly(divinylbenzene) (PDVB), mesophase pitch, poly(4-vinylpyridine) (PVPD), and polyacrylonitrile (PAN). In this contribution, we will focus on PFA, PDVB and mesophase pitch. To induce graphitization, $Fe(NO_3)_3 \times 9H_2O$ was impregnated onto the silica in concentrations between 0

© 2013 WILEY-VCH Verlag GmbH & Co. KGaA, Weinheim

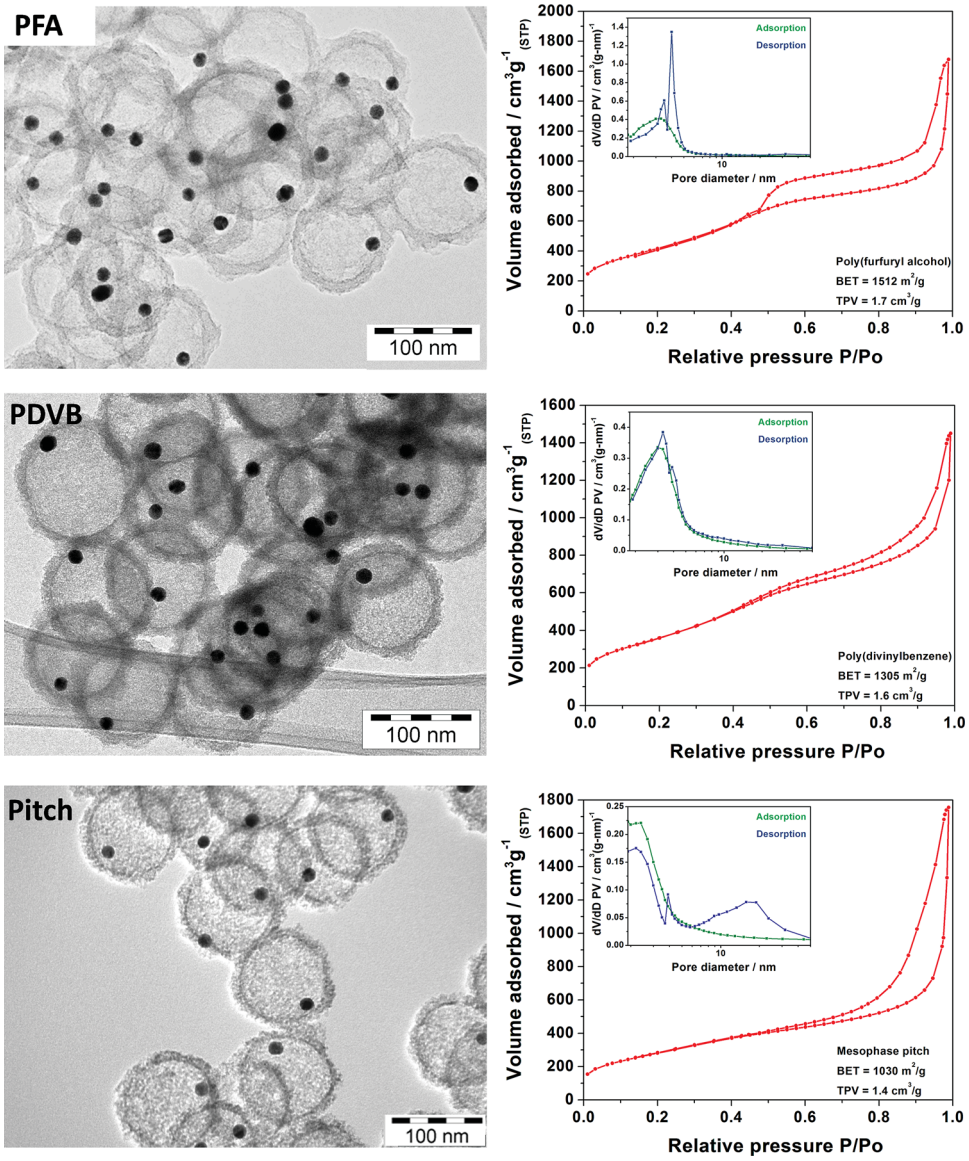

Figure 2. Representative TEM images and corresponding nitrogen sorption isotherms of Au, @C yolk–shell materials produced using different carbon precursors: poly(furfuryl alcohol) (PFA), mesophase pitch, and poly(divinylbenzene) (PDVB). The BJH pore size distributions are shown in the inset figures.

and 8 wt.%. No graphitization catalyst, however, was used in the case of mesophase pitch. Also nickel and cobalt compounds were tested as graphitization catalysts, but iron resulted in the best degrees of graphitization and was thus used in all further experiments. This set of experiments was carried out with 15 nm gold particles as core material, since this system was best explored in the group.

The detailed results of these studies would exceed the scope of this contribution, and thus only the most salient features should be reported here. Overall, PDVB was found to be an optimal carbon precursor, since the resulting carbon spheres had good mechanical stability, suitable porosity and graphitized best of all precursors under the conditions studied (4 h at 1000 °C, 8 wt% iron content). Electron micrographs and sorption isotherms of the products obtained with PFA, PDVB, and mesophase pitch are shown in **Figure 2**.

Au, @C yolk–shell materials derived from PDVB and mesophase pitch have slightly different textural properties compared to the Au, @C material derived from PFA which had been studied previously. In general, all three replicas have high BET surface area and total pore volumes exceeding 1000 $m^2\ g^{-1}$ and 1.4 $cm^3\ g^{-1}$, respectively. While the replica obtained using PFA as carbon precursor has a well-shaped and defined hysteresis loop with a forced closure at ≈0.42 P/P_o due to capillary criticality, the replica using PDVB has a similarly defined adsorption step at a relative pressure of ≈0.4–0.5, but a less pronounced hysteresis loop. The replica obtained with mesophase pitch has a higher fraction of larger mesopores with sizes

© 2013 WILEY-VCH Verlag GmbH & Co. KGaA, Weinheim

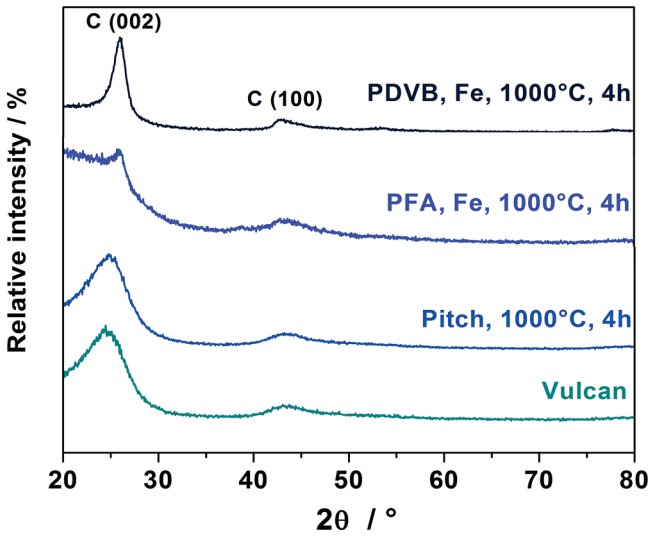

Figure 3. XRD patterns of graphitized carbon spheres. The graphitization was carried out using 8 wt% of Fe using $Fe(NO_3)_3 \cdot 9H_2O$ as catalyst precursor and at 1000 °C for 4 h under nitrogen atmosphere. In the graphic, Fe indicates the graphitization catalyst, which is leached out. Mesophase pitch was graphitized without catalyst. Poly(divinylbenzene) (PDVB), poly(furfuryl alcohol) (PFA), mesophase pitch and carbon black Vulcan for comparison.

between 10 nm and 30 nm. Part of these larger mesopores might be attributed to the incomplete pore filling, which could also explain the slightly lower surface area of this carbon replica compared to the replicas using PFA and PDVB.

With respect to porosity and ease of synthesis, PFA and PDVB would both be suitable as precursor to provide a support for electrocatalysts. However, their graphitization behavior was found to be substantially different. **Figure 3** shows the selected XRD patterns of carbons obtained from the different precursors after thermal treatment at 1000 °C for 4 h with 8 wt% of Fe as graphitization catalyst impregnated onto the silica (the study of various precursors for carbon was carried out using SiO_2@*m*-SiO_2 templates without gold core to facilitate production, thus, there is no reflection of the gold visible in the patterns); the pattern of Vulcan carbon, a typical commercial fuel cell catalyst support, is given for comparison. The PDVB-derived carbon shells clearly show the best degree of graphitization, with a pronounced reflection at 26.5° (2θ), while the other samples are characterized by a broader reflection shifted to lower angles, characteristic of turbostratic carbon. This is also confirmed by Raman spectroscopy (Figure S1, Supporting Information). Since the textural properties and the highly graphitic structure of the PDVB-derived shells appeared to be best suited for the targeted electrocatalysts, this system formed the basis for subsequent experiments.

2.2. Synthesis of Pt, @C

For the development of Pt, @C the same general synthesis approach as used for the synthesis of Au, @C was followed. However, instead of the 15 nm gold particles, the starting material was a platinum colloid of smaller particle size (<5 nm). The influence of different synthesis parameters was studied in order to optimize the production of Pt, @C yolk–shell materials with the highest loading possible and best structural characteristics.

The major difference when using smaller metal particles is the increased surface area. This is not only important for the catalytic reaction, but also during synthesis, since the surface area is crucial in determining the required amount of poly(vinylpyrrolidon) (PVP) which is needed as stabilizer for the metal colloids and as nucleation layer for the formation of silica on the metal colloids. If the same PVP:metal ratio is used as for encapsulation of the gold catalysts, the resulting silica-encapsulated particles are of very low quality, with many Pt-particles encapsulated in one silica sphere and the silica spheres being fused together (Figure S2, Supporting Information). With increasing PVP/Pt-ratio, the quality of the materials gradually improves and is optimized at a ratio of 0.04 (**Figure 4**). At yet higher PVP concentrations, the quality deteriorates again, with

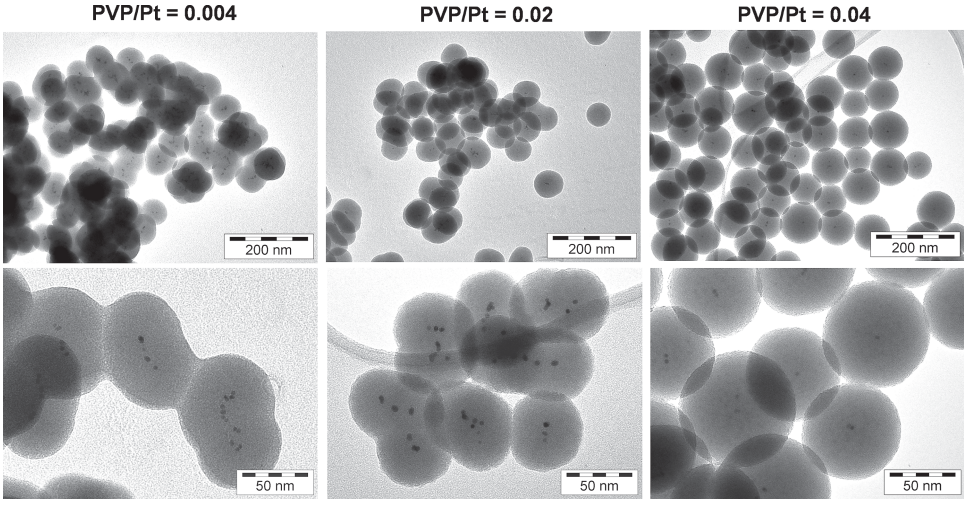

Figure 4. TEM images of representative Pt@SiO_2 core@shell systems prepared using different PVP/Pt molar ratios: left) PVP/Pt = 0.004, middle) PVP/Pt = 0.02, and right) PVP/Pt = 0.04.

© 2013 WILEY-VCH Verlag GmbH & Co. KGaA, Weinheim

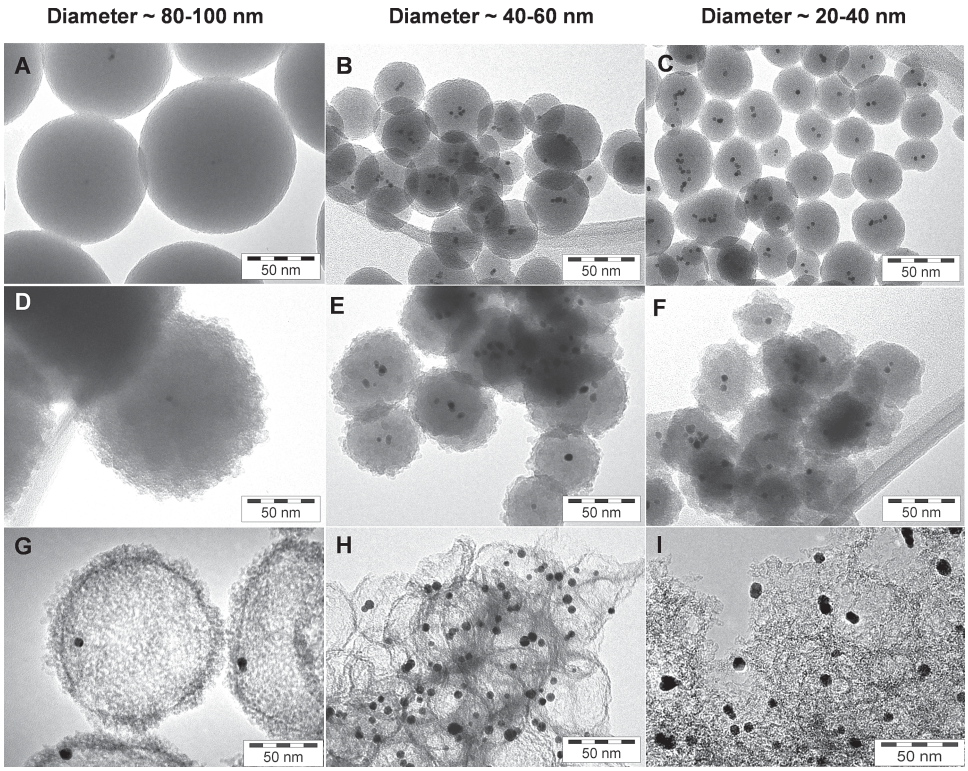

Figure 5. Pt@SiO_2 materials of different diameter, the corresponding D–F) Pt@SiO_2@*m*-SiO_2 materials after the mesoporous silica covering, and the carbon nanocasts G–I) Pt, @C.

the particle sizes of the silica shells becoming inhomogeneous, and again partially more than one Pt-particle incorporated. The ratio of 0.04 was thus used as the basis for the coating with the porous silica shell.

For this coating procedure, a mixture of TEOS and octadecyltrimethoxysilane (OTMS) is used, where the long hydrocarbon chain of the OTMS serves as the porogen. For the coating with the second silica shell, the total amount of mesoporous silica precursors—TEOS and OTMS—was adjusted to obtain a thickness of ≈15 nm, and the ratio between them was adjusted in order to tune the pore structure of the shell. Increasing the TEOS/OTMS molar ratio means a reduction in the amount of porogen, which in turn leads to a reduction in the porosity of the mesoporous silica shell. For the three ratios studied (5, 15, 25), the formation of the mesoporous silica shell around the preformed core@shell particles was successful (Figure S3, Supporting Information). The highest porosity was achieved with a TEOS/OTMS molar ratio of 5. Here a pronounced step in the nitrogen sorption isotherm could be identified between relative pressures of 0.3 and 0.4, the corresponding pore size was determined as 2.8 nm, the BET surface area of the composite was about 440 $m^2\ g^{-1}$, and a pore volume close to 0.5 $cm^3\ g^{-1}$. The values of these textural parameters decreased with increasing ratio of TEOS/OTMS to 2.2 nm, 350 $m^2\ g^{-1}$, and 0.33 $cm^3\ g^{-1}$ for a ratio of 15, and to 1.9 nm, 260 $m^2\ g^{-1}$, and 0.225 $cm^3\ g^{-1}$ for a ratio of 25 (Figure S4, Supporting Information). Attempts to increase porosity using smaller molar ratios than 5 failed, due to insolubility of OTMS at higher concentrations in water. When the concentration of OTMS is further increased, its hydrophobic character plays a predominant role, causing phase separation. To overcome this phase separation problem, the temperature of the system was increased (50 °C). However, a higher temperature resulted in faster hydrolysis/condensation of TEOS alone at the surface of the Pt@SiO_2, without OTMS taking part in the reaction. Therefore, the porosity could not be increased under the reaction conditions used beyond the one achieved at a TEOS/OTMS ratio of 5.

The total size of the Pt@SiO_2@*m*-SiO_2 can be modified by changing the overall amount of silica precursor used, while the ratio of the sizes of the solid and the porous silica shell can be adjusted by changing the amounts of silica precursor used in the different steps. This is illustrated in **Figure 5** for three different sizes. Compared to the standard size of 80–100 nm, the amount of silica precursor in the first step for solid shell production was reduced by 50% (Figure 5, middle) or 85% (left). The total amount of the precursor mixture (TEOS/OTMS = 5) in the shell was reduced by 50% and 70%, respectively. Reduction by 85% in the second step led to such thin porous shells that these materials could not be used further in the carbon nanocasting step. While this series of experiments shows that the sizes can be adjusted, the quality of the smaller particles is somewhat reduced. The probability to encapsulate more than one platinum particle is increased, and also the polydispersity is higher at lower total sphere size.

The different Pt@SiO_2@*m*-SiO_2 templates were used for nanocasting of carbon shells using PDVB as carbon precursor, for the reasons which are discussed in the previous section. The first set of exotemplates was the series of materials of ≈100 nm

© 2013 WILEY-VCH Verlag GmbH & Co. KGaA, Weinheim

sphere diameter, which had been synthesized with different molar ratios TEOS/OTMS. The nanocasting of the carbon shell using the exotemplates prepared with molar ratios TEOS/OTMS of 15 and 25 led to the formation of rather poor quality materials with most of the resulting carbon shells broken. Only the exotemplate prepared with a molar ratio TEOS/OTMS of 5 was suitable for the production of a well developed replica. High interconnectivity of the mesopore system in the exotemplate is obviously mandatory for the successful carbon shell replication. Only with a well interconnected pore structure the monomers can be polymerized to form a continuous network that withstands the carbonization and leaching process.

Figure 5 (lower row) shows representative TEM micrographs of the carbons replicated from the differently sized spheres described above. In general, using the exotemplate with 80–100 nm total diameter, well shaped replicas were obtained; however, some defective particles were also present, most probably due to morphological defects in a fraction of the exotemplate spheres. The carbon shell replica obtained from the 80–100 nm templates has a BET surface area and total pore volume of ≈900 m^2 g^{-1} and 1.4 cm^3 g^{-1}, respectively. The synthesis of the carbon shells using smaller exotemplates was not as successful as for the standard material of ≈100 nm, as is obvious from Figure 5. For the 40–60 nm exotemplate, only poorly replicated carbon shells are observed over the whole material, and only some single yolk–shell structures are present. Most of the shells are broken and seem to be agglomerated. In the case of the 20–40 nm templates, not even clear carbon shells are found, but instead a continuous matrix of carbon is observed. The Pt nanoparticles are separated from each other by the carbon network, but no single yolk–shell structures are visible. The reasons of the poor replication can be either associated with the strong agglomeration of the exotemplate particles when the particle size is significantly reduced, or with the lower thickness of the mesoporous silica shell. The impregnation/carbonization steps were carried out as described above, that is, PDVB in the presence of iron compounds as graphitization catalysts. As for the samples with the gold-cores, this led to the formation of highly graphitic carbon structures. The XRD pattern shows similar reflections characteristic for graphitic carbon as given in Figure 3, in addition, broad reflections of the small Pt-particles are present.

Atomic absorption spectroscopy (AAS) was used to analyze the platinum concentration in the different samples. For the large, rather well developed Pt, @C particles with a size of 100 nm, the platinum concentration is only 2 wt%, the smaller templates lead to materials with platinum contents of 5 wt% and 8 wt%, respectively. These concentrations are much too low for useful electrocatalysts; commercial fuel cell catalysts have platinum concentrations that can exceed 50 wt% in order to achieve high activity. Reaching such high platinum loadings (and correspondingly high platinum surface areas) by reducing the shell size, while maintaining good encapsulation of individual particles, does not appear possible following this synthesis pathway. In addition, the carbon encapsulation of the small platinum particles with a size of 3.5 nm is not straightforward and only works in a narrow parameter range. Thus a different way of improving the catalysts was investigated, i.e. encapsulation of bimetallic Au@Pt core–shell particles of larger particle sizes in order to produce uniform exotemplate particles as well as to maximize platinum surface area.

2.3. Synthesis of AuPt, @C

This synthetic pathway was chosen to combine the ease of encapsulation of gold particles with a size of 15–20 nm with the electrocatalytic properties of platinum which is coated as a shell on the gold particles. The synthesis of the core@shell Au@Pt colloid is based on a seed-growth formation mechanism with modification of the reducing agents.[34] First, the gold colloid is synthesized by citrate reduction, as described above. After the Au colloid formation, the citrate ions act as protecting agent, and at the same time serve as coupling species for the selective adsorption of Pt salt precursor at the surface of the Au nanoparticles. Afterwards, the reduction of the Pt salt precursor leads to a metallic Pt shell around the gold nanoparticle core. The formation of the Pt shell requires a careful control of the reduction conditions, particularly time, temperature and reducing agent. After the formation of the Au nanoparticles, the Pt precursor –hexachloroplatinic acid- was added to the aqueous Au colloidal solution and was let to adsorb under stirring at room temperature for 2 h. The reduction of the Pt precursor was carried out using either sodium citrate or sodium boronhydride in stoichiometric amounts with respect to the Pt. The reduction of the Pt precursor using sodium citrate was carried out with the remnant citrate in the medium after the Au colloid formation under reflux for 1 h, but did not lead to full reduction of the platinum. After separation of the colloids, the supernatant was still slightly orange, indicating the presence of platinum in solution. EDX analysis of several AuPt particles gave Au:Pt atomic ratios of approximately 6:1 for a nominal Au:Pt ratio of 1:1, 4:1 for a nominal ratio of 1:2, and 1:1.8 for a nominal ratio of 1:3. The ratio of 1:1.8 was also confirmed by bulk analysis using AAS. Substitution of citrate against $NaBH_4$ as reducing agent led to higher levels of platinum recovery; however, the majority of the platinum was formed as separate nanoparticles and not deposited onto the gold nanoparticles. Increasing the reflux time in the citrate reduction led to slightly higher platinum yields; however, there was also an increased level of coagulation/precipitation, so that for further experiments the colloids synthesized with a Au:Pt nominal ratio of 1:3 after one hour refluxing were used.

The silica encapsulation/carbon nanocasting of these Au@Pt particles followed the same procedure as discussed previously. The Au@Pt colloid was first functionalized with PVP for subsequent covering with the non-porous silica/mesoporous silica double shell, then the solid and the mesoporous shell were grown on the metal particles, and the composite was finally calcined at 550 °C under air. **Figure 6** shows representative TEM images and nitrogen sorption isotherms of the exotemplate Au@Pt@SiO_2@*m*-SiO_2 and the corresponding replica AuPt, @C materials. The graphitization of the carbon shell was assisted by Fe, as discussed above. The total diameter of the Au@Pt@SiO_2@*m*-SiO_2 can be tuned by changing the amount of silica precursors as described for the previous systems. Figure 6 reveals that not only the exotemplate particles, but also the yolk–shell replicas have uniform particle sizes of around

© 2013 WILEY-VCH Verlag GmbH & Co. KGaA, Weinheim

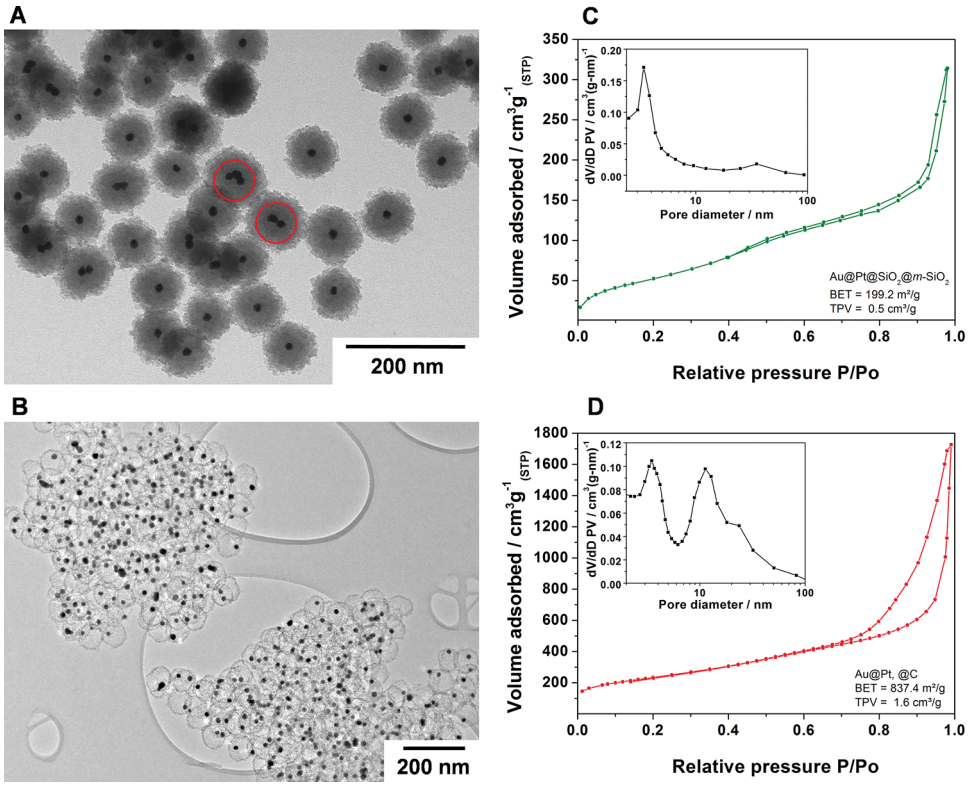

Figure 6. TEM images, nitrogen sorption isotherms, and corresponding desorption BJH pore size distributions (inset) of: A,C) Au@Pt@SiO_2@*m*-SiO_2 core@shell material and B,D) corresponding AuPt, @C yolk–shell material after leaching of the silica. Au:Pt theoretical molar ratio 1:3.

70 nm. Some of the bimetallic cores have bigger particle size, which is due to initial encapsulation of two—and, seldom, more—bimetallic nanoparticles in the same silica exotemplate particle. However, most shells contain only one core. The pores in the shell are smaller than the metal particles, so that encapsulation is effective to prevent particle coalescence.

Since the synthesis of the AuPt, @C yolk–shell particles involves several thermal treatment steps (550 °C for the synthesis of the porous silica shell, 1000 °C for carbonization/graphitization), the microstructure of the bimetallic core is expected to change during processing. These changes were tracked by spatially resolved elemental analysis, XRD and XPS. **Figure 7** shows the XRD patterns of a typical sample after different treatment steps, in addition, the pattern of the pure Au, @C, discussed in the first section, is given. The diffraction pattern of Au, @C (carbonized at 1000 °C) presents the typical reflections of the face-centered cubic (fcc) Au crystal structure. In contrast, in the powder diffraction pattern of the Au@Pt@SiO_2@*m*-SiO_2 core–shell particle after calcination at 550 °C (blue trace), the reflections corresponding to the Au seed can not clearly be observed. Instead an asymmetric reflection corresponding to the fcc Pt crystal structure is observed. This asymmetric reflection results from the overlapping of the Pt shell reflections and the Au core, which may be poorly crystalline. Alternatively, the Au crystalline domain sizes may be significantly smaller than the particle size. Here, it is important to note than the Au, @C comparison materials was thermally treated to 1000 °C during the carbonization process, which may have a strong influence on the crystallinity of the Au core. The patterns of the samples after the carbonization of the polymer composite at 1000 °C under nitrogen atmosphere and after leaching of the silica are quite similar: in both powder diffraction patterns, a set of reflections associated to a gold phase are visible. The reflections of this Au phase are, however, all shifted to higher diffraction angles compared to pure gold, which might be associated to the formation of an AuPt alloy at the interface of the Au and Pt phases or in the core. Note that the graphite reflections are often not visible at such high metal loadings.

The different crystalline phases present in the AuPt, @C material after heat treatment at 1000 °C were analyzed by Rietveld refinement. According to this, the bimetallic core is composed of 40 wt% Au and 60 wt% Pt, corresponding well to the Au:Pt ratio of 1:1.8 determined by EDX and AAS, considering the error margins of the methods. The lattice parameters given by the National Bureau of Standards for pure Au and Pt are 4.0786(9) Å and 3.9231(3) Å, respectively. The lattice parameters determined for the AuPt, @C system are 4.0466(1) Å and 3.9258(1) Å for Au and Pt, respectively. In the case of Pt, the lattice parameters are in completely agreement with the reported value. However, in the case of Au the lattice parameters are smaller than expected. This change in the lattice parameters of Au can be associated either with the incorporation of Pt in the Au fcc crystal structure (alloy formation), an influence of the particle size, or to strain contributions.[35] According to literature results,[36–38] in the case of a AuPt alloy formation the

© 2013 WILEY-VCH Verlag GmbH & Co. KGaA, Weinheim

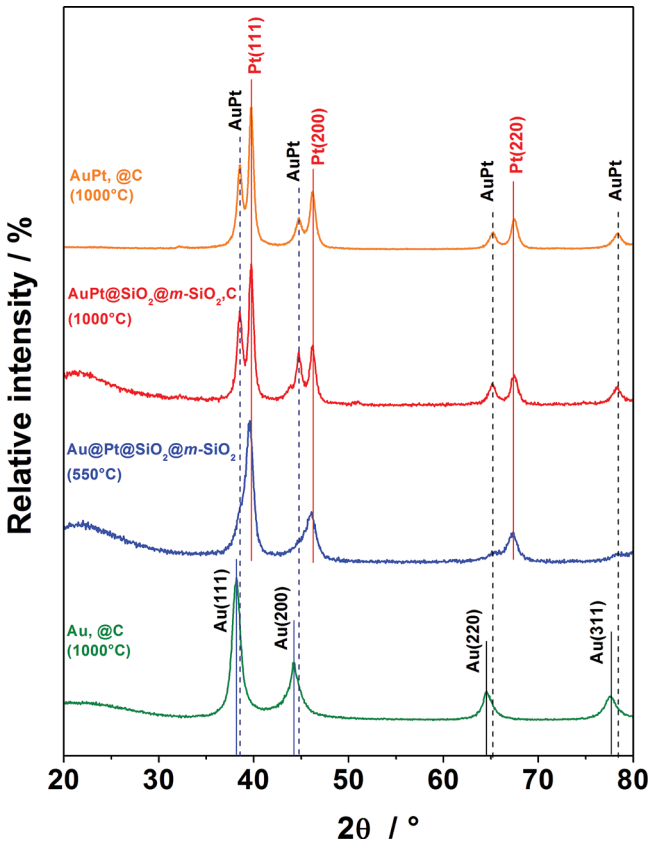

Figure 7. XRD powder patterns of the different materials involved in the synthesis of the AuPt, @C yolk–shell material. The maximum temperature at which each material was treated corresponds to the value in parenthesis.

determined lattice parameter 4.0466(1) Å would correspond to an incorporation of ≈20% of Pt in the Au crystal structure.

The spatial distribution of the gold after the different treatment steps was analyzed by EDX line scans. After the encapsulation in the silica shells, a clear core–shell structure with a gold core and a platinum shell can be identified (**Figure 8**). However, after thermal treatment at 1000 °C to induce carbonization/graphitization, phase separation between the gold and platinum seems to occur (**Figure 9**). Many particles were studied by EDX, and such a platinum-gold distribution was observed for most of them. In few cases, an apparently homogeneous distribution was recorded. This, however, is probably due to an unfavorable orientation of the particles in the TEM beam. The thermally induced phase segregation of AuPt alloys has been studied by experimentalists and also theoreticians. It has already been shown that a carbon-supported gold-platinum bimetallic catalyst ($Au_{22}Pt_{78}$/C) of ≈6 nm underwent phase segregation at temperatures higher than 500 °C, indicated by the observation of lattice parameters of single phase Pt and Au in XRD.[39] Thermodynamic analyses have correlated this segregation behavior to the significant difference in surface free energy between Au (1.50 J m^{-2}) and

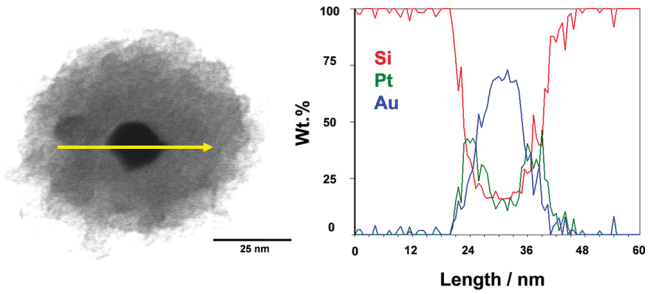

Figure 8. EDX line-scan profile of Au@Pt@SiO_2@*m*-SiO_2 core@shell particle after thermal treatment to 550 °C. Color code of EDX line profiles: blue corresponds to Au, green to Pt, and red to Si. The yellow arrow indicates the direction of the scan.

Pt (2.48 J m^{-2}).[40] This difference favors the formation of an Au-enriched outer shell whereas the Pt concentration is enriched in the core region, in order to reduce the overall surface energy of the system at high temperatures. At high temperature, the gold would thus tend to move from the core of the particles to the outer surface which could lead to the restructuring observed.

Nevertheless, while a pronounced core–shell structure with platinum enriched in the outer shell is probably not present after high temperature treatment in the AuPt, @C composites, the platinum loading of around 30 wt% achieved using this synthetic pathway suggested sufficiently high electrocatalytic activity to carry out electrocatalytic studies on these catalysts. Moreover, XPS data of the AuPt, @C samples revealed that platinum was present in the zerovalent state in the catalysts (Figure S5, Supporting Information), a mandatory requirement for high electrocatalytic activity. Quantification of the gold and platinum concentration on the surface of the particles was not possible due to encapsulation in the carbon shell, which in spite of its porosity captures a significant fraction of the photoelectrons from the metal core. Nevertheless, pronounced and intense signals of both gold and platinum were detected.

3. Electrochemical Stability Investigations of AuPt, @C

AuPt alloy nanoparticles have recently been investigated in the field of electrocatalysis. Some reports have suggested improved catalytic properties in the oxygen reduction reaction (ORR)[39,41–45] and methanol oxidation reaction (MOR).[46–50] The focus of this work, however, is the possible stabilization effect brought about by the encapsulation strategy. In order

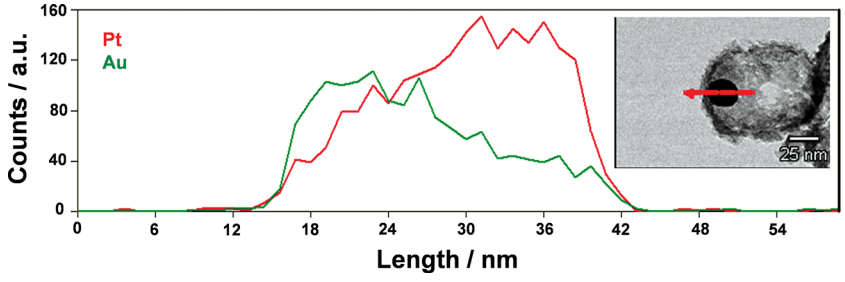

Figure 9. EDX line scan of AuPt, @C yolk–shell particle after thermal treatment at 1000 °C.

© 2013 WILEY-VCH Verlag GmbH & Co. KGaA, Weinheim

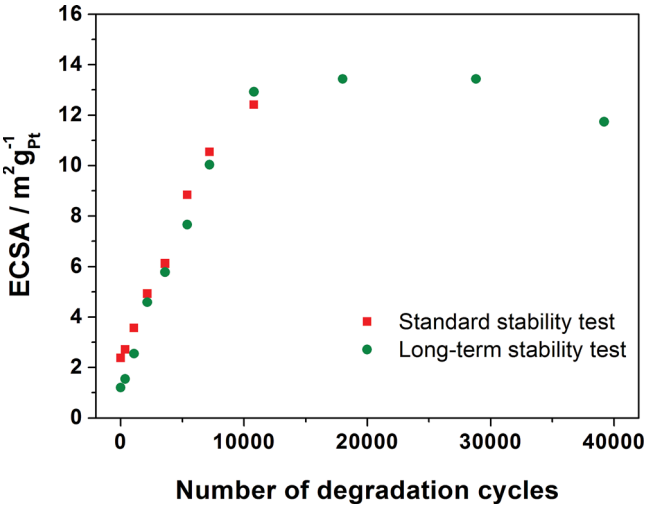

Figure 10. Electrochemical stability test under ex-situ conditions (RDE measurements). Pt surface area change for AuPt, @C yolk–shell material during the ex-situ degradation test (with 30 μg_{Pt} cm^{-2} at the working electrode).

to test for possible advantages of the carbon shell, a series of electrochemical degradation tests were performed for the AuPt, @C yolk–shell material described in the previous section. The accelerated electrochemical degradation tests were performed in a three-electrode electrochemical cell under the conditions given in the Experimental Section. The degradation protocol consisted in a series of potential cycles between 0.4 and 1.4 V_{RHE} (without rotation of the RDE) with a scan rate of 1 V s^{-1}, which is intended to simulate the detrimental start-stop conditions of a fuel cell under operation (note that in the literature the upper threshold for stability tests often is only 1.0 V), and which included periodical determination of the platinum electrochemical surface area (ECSA) by electrochemical oxidation of a pre-adsorbed CO monolayer (CO-stripping measurements).

Figure 10 shows the evolution of the electrochemical surface area (ECSA) as a function of the number of degradation cycles during standard (10 800 cycles) and long-term (39 200 cycles) stability tests. In both cases, a rather slow increase in ECSA is observed in the initial phase, then—particularly in the long-term stability test—the ECSA reaches a plateau. This long-term activation behavior is quite intriguing, since after 10 800 cycles standard Pt/Vulcan materials, of smaller particle size, would have already lost ≈70% of the Pt surface area under the same potential cycling conditions.[26] This long activation process is also reflected in the CO-stripping curves at different stages of the degradation test (Figure S6, Supporting Information). Only after 1080 cycles it is possible to detect a small peak, suggesting that until that point the catalyst is completely shielded from CO adsorption and consequently does not show electrochemical activity. The highest CO-stripping peak is detected after 18 000 cycles and only after 39 200 cycles the ECSA slightly decreases. If the potential cycles needed for the activation of the catalyst (10800 CVs) are subtracted from the total number of potential cycles, the catalyst has completely stable activity during the remaining 28 400 start–stop cycles.

For an average particle size of 20 nm with a loading of 30 μg_{Pt} cm^{-2} on the electrode (0.196 cm^2 area of the electrode), a theoretical ECSA of 14 m^2 g^{-1} is calculated, assuming spherical nanoparticles and the average of the densities of Au and Pt (neglecting the contact area with the support). This theoretical value for the ECSA is in good agreement with the maximum surface area obtained after the activation process. One may thus conclude that after the activation process of 10 800 potential cycles a substantial fraction of the surface is accessible for electrochemical reaction.

In order to understand the electrochemical behavior of the AuPt, @C yolk–shell catalyst, identical-location transmission electron microscopy (IL-TEM) investigations were conducted to detect changes of the single yolk–shell particles during electrochemical cycling. The IL-TEM measurements were performed at the beginning of the aging experiments and after 10 800 start–stop cycles, because this should reveal the most pronounced changes. IL-TEM measurements were carried out on multiple locations in order to draw statistically meaningful conclusions.

Figure 11 shows one particular location where significant changes can be observed after 10 800 potential cycles. The TEM images in the top row show the AuPt, @C yolk–shell particles before the electrochemical degradation test, and in the bottom row the corresponding identical locations after 10 800 potential cycles between 0.4–1.4 V_{RHE}. In this particular spot, it can be observed that the main effect of the potential cycling is the degradation of the carbon shell. The shrinkage of the carbon shells and the reduction of the thickness in some regions of the carbon shells can clearly be detected, if one compares with the corresponding pristine states. On the other hand, no obvious change in the size or morphology of the bimetallic core is observed.

Higher magnification TEM images of the yolk–shell particle in Figure 11A,D are shown in Figure 11B,E. Although the contrast between the carbon film of the TEM grid and the carbon shell is rather poor, due to the low thickness of the carbon shells, it is possible to observe that after electrochemical degradation treatment the carbon shells are even thinner, up to the point that in some areas they seem to be indistinguishable from the carbon film (zones pointed at with the blue arrow). The same effects are observed for the particle in the middle, magnified in Figure 11C,F. Near this particle it is also possible to see that the carbon zone where the AuPt particle is located, has completely vanished after the degradation test (red arrows). These results strongly suggest that during the first 10 800 activation/degradation cycles the accessibility to the AuPt core is promoted by the partial degradation of the carbon shell.

One should note, however, that there are other regions of the sample where the apparent differences before and after degradation are much less pronounced (Figure S7, Supporting Information). In some spots, also bimetallic particles are present which are located outside of the carbon shells. However, their concentration seems to be so low that they do not determine the overall macroscopic behavior of the samples.

It is unfortunately impossible to synthesize a suitable reference catalyst in order to compare the degradation behavior of an encapsulated and non-encapsulated AuPt catalyst. The carbon shells are mechanically so stable that they can not be destroyed

© 2013 WILEY-VCH Verlag GmbH & Co. KGaA, Weinheim

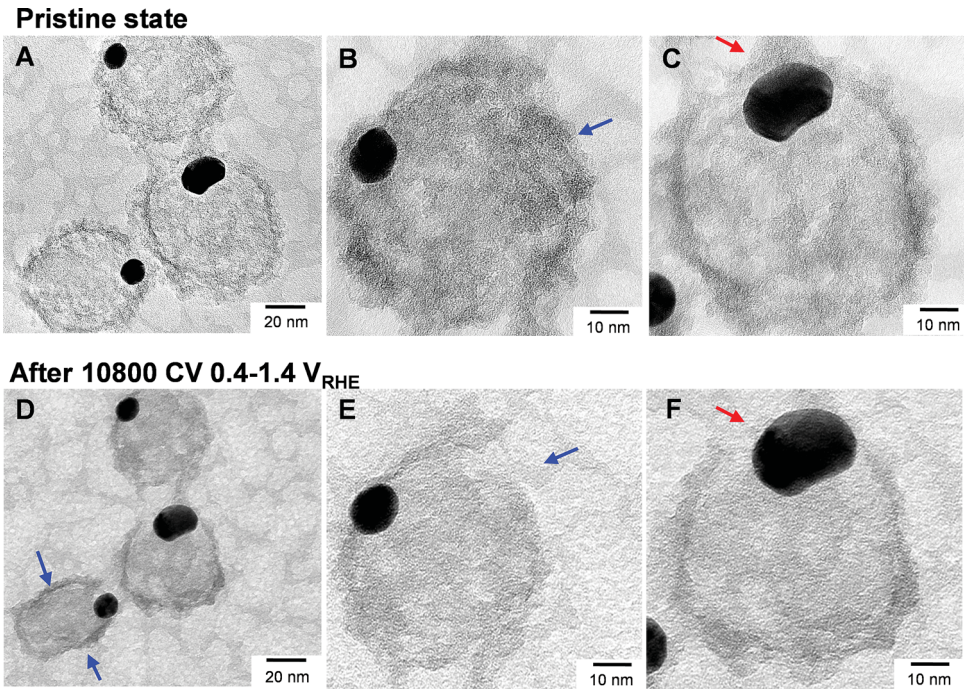

Figure 11. IL-TEM images of AuPt, @C yolk–shell in A–C) the pristine state and D–F) after 10 800 electrochemical degradation cycles between 0.4 and 1.4 V_{RHE} with a scan rate of 1 V s^{-1} in argon saturated 0.1 M $HClO_4$ at 25 °C.

by milling or pressing. An AuPt/Vulcan catalyst can also not be synthesized as a reference, since the metal particles are not stable at the sintering temperature of 1000 °C which is part of the synthetic protocol for the core–shell catalyst. Nevertheless, the almost complete absence of any indication of activity/surface area loss during almost 30 000 harsh accelerated degradation cycles demonstrates that the encapsulation concept for fuel cell catalysts contributes to the exceptional stability against degradation.

4. Conclusions

An encapsulation strategy for the stabilization of noble metal electrocatalysts is described, in which pre-formed nanoparticles are incorporated first in a solid/mesoporous silica shell which is subsequently used as hard template for the formation of graphitic carbon. Leaching of the silica results finally in the yolk–shell catalyst. The carbon shell production was first optimized for the known 15 nm gold cores. Then the synthesis was extended and optimized for 3.5 nm platinum nanoparticles as cores. Since the synthesis window for these catalysts was rather narrow, and the achievable loading was relatively small (only about 2% Pt for well preserved core–shell particles), coating of the 15 nm gold particles by a platinum shell was finally used for the production of the electrocatalysts. Although separation of the platinum and the gold phase occurred after 1000 °C treatment for graphitization/carbonization, the catalysts were shown to be electrochemically active in *ex-situ* measurements after an unusually long activation period. This activation period is probably due to removal of carbon on the surface of the metal particles to make them accessible. After this activation, the catalysts show exceptional stability for almost 30 000 harsh degradation cycles between 0.4 V and 1.4 V_{RHE}.

While the synthetic pathway used, due to its complexity, is certainly not applicable for the production of practically useful electrocatalysts, and the platinum size needs to be reduced further in order to achieve high platinum mass activity, the results demonstrate that encapsulation of the catalytically active metal particles in porous, graphitic shells is a suitable method for the generation of stable electrocatalysts. Future work along these lines will require simplification of the synthesis protocols (continuously operated tubular reactors or gas phase processes could be suitable approaches), reduction of the platinum particles sizes, and/or the use of base metal core/platinum shell nanoparticles to achieve high platinum surface area while minimizing overall platinum consumption. The materials discussed in this work could provide the blueprint for such advanced catalyst systems.

5. Experimental Section

Synthesis of Au, @C Yolk–Shell Material (Standard Material with Approximately 100 nm Size): In a typical preparation, 212.5 mL of millipore water (18.2 MΩ cm^{-2}) was vigorously stirred under reflux and a $HAuCl_4$ solution (0.5 mL of Au^{3+} solution (≈0.25 M) in 24.5 g of millipore water) was added. Once the boiling point of the solution was reached again, a sodium citrate solution (0.250 g citric acid trisodium salt bihydrate dissolved in 12.5 g of millipore water) was added. The system was refluxed for 30 min, and finally the resultant colloidal solution was allowed to cool down to room temperature, followed by the addition of a PVP solution (1.35 mL, 6 mg mL^{-1}; solvent millipore water). The resultant mixture was stirred for 24 h to allow complete

© 2013 WILEY-VCH Verlag GmbH & Co. KGaA, Weinheim

adsorption of the PVP on the gold surface. Afterwards, the solution was centrifuged (10 000 rpm; 50 min), the supernatant was removed, and the concentrated colloid was then adjusted to 12 g by addition of millipore water. The colloidal solution was vigorously stirred for 10 min, followed by addition of ethanol (50 g) premixed with concentrated ammonia solution (1.68 mL, 28–30%). Afterwards, a solution of 2.37 mL of TEOS (98%) was added. The reaction mixture was then stirred for additional 12 h at room temperature. Afterwards, a mixture of TEOS and OTMS was added drop wise during 20 min (1.08 mL of TEOS, 0.44 mL OTMS; molar ratio TEOS/OTMS = 5). After the addition of the precursors the stirring was stopped and the system was allowed to react for 6 h. Subsequently, the solvent was removed by centrifugation (8000 rpm; 10 min) and the product was dried at 70 °C overnight. Finally, the material was calcined in air by heating the system from room temperature to 550 °C with a heating rate of 2 °C min^{-1} followed by natural cooling to room temperature.

The resulting Au@SiO_2@*m*-SiO_2 exotemplate (total diameter ≈100 nm) was evacuated under vacuum for 1 h. After the evacuation the material was kept under argon for 30 min. Afterwards, the pore structure was filled with DVB/AIBN (35:1 molar ratio) mixture via the incipient wetness method. The volume of the DVB/AIBN solution added to the solid was exactly the total pore volume of the sample calculated from the nitrogen sorption isotherm of the exotemplate at 0.95 relative pressure. To the degassed material, placed in a glass flask, the total amount of DVB/AIBN solution was added in three steps. In every step the solution was added drop wise and the solid was vigorously shaken by hand and forcefully crushed with a spatula against the internal wall of the glass flask for about 10 min. The closed glass with the impregnated exotemplate was placed in a Schlenk flask with Ar, where the polymerization of the monomer was carried out for 24 h at 75 °C. Afterwards, the polymer composites were carbonized in a tube-oven under nitrogen at 1000 °C with heating rate of 5 °C min^{-1}.

The silica exotemplate was removed by leaching out with an aqueous solution of 1 M NaOH for 24 h under stirring at 50 °C. The resulting yolk–shell material was washed four times with distilled water and once with ethanol using centrifugation to separate the solid from the liquid phase (9000 rpm; 15 min) each time. Finally, the material was dried in air overnight at 70 °C.

Synthesis of Pt, @C Yolk–Shell Material with a Size of Approximately 80–100 nm: In a typical preparation 90 g of ethanol (analytical grade), 6 mL of $H_2PtCl_6 \cdot xH_2O$ solution (2.52×10^{-2} M) and the corresponding amount of a PVP solution [6.25×10^{-3} M; 3.4 g PVP (M_w: 55 000 g mol^{-1}) dissolved in 10 mL of millipore water under strong ultrasonication] were vigorously stirred and heated under reflux for 4 h. After the dark brown colloid was left to cool down to ambient temperature, 450–650 mL of acetone (technical grade) were added for the precipitation of the colloid. First 450 mL were added and the mixture was centrifuged (13 000 rpm, 20 min). If the supernatant presented a strong brown color, additional of 50 mL was added to improve the precipitation process. The precipitated colloid consisted of a solid stuck to the centrifuge tubes. To re-disperse the colloid, 16 g of water was added to the colloid and the mixture was vigorously ultrasonicated until complete redispersion of the solid particles. The aqueous colloidal solution was mixed with 100 g of ethanol (analytical grade), 3.36 mL ammonia (28–30%), and finally 4.74 mL of TEOS (98%) were added under stirring. The reaction was left to proceed at room temperature for 12–16 h (overnight). Afterwards, a mixture of TEOS/OTMS (for a molar ratio equal to 5, 3.46 mL of TEOS and 1.32 mL of OTMS were used) was drop-wise added to the reaction vessel for ca. 20 min. When the addition was finished, the stirring was stopped and the reaction was continued for 4 h. Subsequently, the solvent was removed by centrifugation (8000 rpm; 10 min) and the product was dried at 70 °C overnight. Finally, the material was calcined in air by heating the system from room temperature to 550 °C with a heating rate of 2 °C min^{-1} followed by natural cooling to room temperature. The resulting Pt@SiO_2@*m*-SiO_2 exotemplates were used for the nanocasting of the carbon shell following the same protocol as described above for the Au@SiO_2@*m*-SiO_2 system, using DVB as carbon precursor.

Synthesis of AuPt, @C Yolk–Shell Material: In a typical preparation 212.5 mL of millipore water (18.2 MΩ cm^{-2}) was vigorously stirred under reflux and a $HAuCl_4$ solution (0.5 ml of Au^{3+} solution (≈0.25 M) in 24.5 g of millipore water) was added. Once the boiling point of the solution was reached again, a sodium citrate solution (0.250 g citric acid trisodium salt bihydrate dissolved in 12.5 g of millipore water) was added. The system was refluxed for 30 min, and finally the resultant colloidal solution was allowed to cool down to room temperature. Afterwards, 0.2145 g of hexachloroplatinic acid hexahydrate dissolved in 1 mL of millipore water was added to the Au colloid (for the ratio of Au:Pt of 1:3) and was left under stirring for 1 h. Afterwards, the solution was refluxed for 1 h more for the reduction of the Pt precursor. In this step, the colloidal solution changes from dark red to deep violet-reddish color. Subsequently, the Au@Pt colloid was cooled down naturally to ambient temperature, and finally 1.35 mL of PVP solution (6 mg mL^{-1}; solvent millipore water) was added and was left under stirring overnight.

The resulting Au@Pt colloid was centrifuged (10000 rpm; 50 min), the supernatant was removed, and the concentrated colloid was then adjusted to 12 g by addition of millipore water. The colloidal solution was vigorously stirred for 10 min, followed by addition of ethanol (50 g) premixed with concentrated ammonia solution (1.68 mL, 28–30%). Afterwards, 2.37 mL of TEOS (98%) was added. The reaction mixture was then stirred for additional 12 h at room temperature. Afterwards, a mixture of TEOS and OTMS was added drop wise during 20 min (1.41 mL of TEOS, 0.57 mL OTMS; molar ratio TEOS/OTMS = 5). After the addition of the precursors the stirring was stopped and the system was allowed to react for 6 h. Subsequently, the solvent was removed by centrifugation (8000 rpm; 10 min) and the product was dried at 75 °C overnight. Finally, the material was calcined in air by heating the system from room temperature to 550 °C with a heating rate of 2 °C min^{-1} followed by natural cooling to room temperature. The resulting Au@Pt@SiO_2@*m*-SiO_2 exotemplates were used for the nanocasting of the carbon shell following the same protocol as described above for the Au@SiO_2@*m*-SiO_2 system, using DVB as carbon precursor.

For a graphitized sample, 1 g Au@Pt@SiO_2@*m*-SiO_2 exotemplate (with total pore volume of ≈0.33 cm^3 g^{-1} at P/Po = 0.95) was impregnated with 0.66 mL of a solution of iron (III) nitrate nonahydrate $Fe(NO_3)_3 \cdot 9H_2O$ 2 M in ethanol. The slurry was dried for 12 h at 75 °C. The resulting exotemplate/catalyst material was used for the nanocasting of the carbon shell following the same protocol as described for the Au@SiO_2@*m*-SiO_2 system, using DVB as carbon precursor.

Electron Microscopy: TEM images were obtained on Hitachi H-7500 and HF-2000 instruments. The H-7500 microscope was operated at a maximum acceleration voltage of 120 kV. The HF-2000 instrument is equipped with a cold field emitter and can be operated at a maximum acceleration voltage of 200 kV. Typically, the samples were placed on a Lacey carbon film supported by a copper grid. HR-SEM, BF-STEM, and EDX line profiles were measured on a Hitachi S-5500 ultra-high resolution cold field emission scanning electron microscope. The instrument was operated at a maximum acceleration voltage of 30 kV. The samples were prepared on Lacey carbon films supported on a 400 mesh copper grid. IL-TEM measurements were carried out using a 5 mL drop of 1:5 dilute catalyst suspension deposited on a gold finder grid (NHA7, Plano) coated with a carbon film (Quantifoil R2/2). The catalyst deposited on the TEM grid was treated electrochemically by immobilizing the gold finder grid on the glassy carbon disc working electrode with the help of a Teflon cap. The experiment was designed analogous to the macroscopic degradation study with a total of 10800 cycles between 0.4 and 1.4 V_{RHE} at a sweep rate of 1 V s^{-1} without rotation and without intermediate CO stripping experiments. A more detailed description of IL-TEM studies is given in ref.[30]

Ex-Situ Half-Cell Electrocatalytic Measurements: The electrochemical measurements were conducted at room temperature in a 150 mL Teflon three-compartment electrochemical cell, using a rotating disk electrode (RDE) setup, a Gamry Reference 600 potentiostat, and a Radiometer Analytical rotation controller. The potentiostat, the rotator and the gas flow were automatically regulated using an in-house-developed LabVIEW software.[51] A graphite rod was employed as the counter electrode (CE),

© 2013 WILEY-VCH Verlag GmbH & Co. KGaA, Weinheim

and a saturated Ag/AgCl Electrode (Metrohm) served as reference (RE). However, all potentials are given with respect to the reversible hydrogen electrode (RHE) potential, which was experimentally determined for each measurement. The reference electrode compartment was separated from the main compartment with a Nafion membrane to avoid contamination with chlorides during activity and stability tests.

Stability measurements were performed in 0.1 M $HClO_4$. The electrolyte was prepared with ultrapure water and conc. $HClO_4$ (Merck, Suprapur). Solution resistance was compensated in all electrochemical measurements via positive feedback. The residual uncompensated resistance was less than 4 Ω in all experiments. The catalyst powders were dispersed ultrasonically in ultrapure water (18 MΩ, Millipore) for at least 45 min initially and again for at least 10 min prior to pipetting onto the working electrode (WE) glassy carbon discs (5 mm diameter, 0.196 cm^2 geometrical surface area). The catalysts were dried under air or under mild vacuum.

Measurements were performed at a loading of 30 μg_{Pt} cm^{-2} at the electrode in order to obtain thin and well dispersed catalyst films. Ex-situ aging tests consisted of 10 800 or 39 200 potential cycles (triangular wave) between 0.4 and 1.4 V_{RHE} with a sweep rate of 1 V s^{-1}. Cleaning of the catalyst surface was not performed before starting the degradation test, in order to follow the changes of the Pt surface area from the beginning. The surface area was determined via electrochemical oxidation of adsorbed carbon monoxide (CO-stripping). In each CO-stripping experiment, carbon monoxide was adsorbed on the catalyst in a potential region (e.g., 0.05 V_{RHE}) at which no CO oxidation occurs, until the saturation coverage was reached. Afterwards the electrolyte was purged with argon again until all remaining carbon monoxide was removed from the electrolyte, while the same potential was held. Finally, pre-adsorbed CO was electrochemically oxidized and the charge corresponding to the CO oxidation was measured by the area of the oxidation peak. A more detailed description of general features of CO-stripping curves can be found in the literature.[52]

Experimental details on XRD and sorption analysis can be found in the Supporting Information.

Supporting Information

Supporting Information is available from the Wiley Online Library or from the author.

Acknowledgements

Funding by the DFG in the AIF-DFG Cluster "Innovative Materialien und Verfahren für MT-PEM-Brennstoffzellen" is gratefully acknowledged, in addition to the funding of the Max-Planck-society. J.C.M. acknowledges funding by a Kekulé fellowship from the FCI.

Notes:

[1]The nomenclature used here indicates the innermost component first, separated with an "@" from the first shell, possible additional shells are separated by "@" again; if there is empty space in the core, i.e., a yolk–shell material, this is indicated by a blank, separated by a "," from the core material)

Received: July 2, 2013
Revised: September 6, 2013
Published online: August 10, 2013

[1] P. M. Arnal, M. Comotti, F. Schüth, *Angew. Chem. Int. Ed.* **2006**, *45*, 8224.
[2] S. H. Joo, J. Y. Park, C.-K. Tsung, Y. Yamada, P. Yang, G. A. Somorjai, *Nat. Mater.* **2009**, *8*, 126.
[3] M. Feyen, C. Weidenthaler, R. Güttel, K. Schlichte, U. Holle, A. H. Lu, F. Schüth, *Chem. Eur. J.* **2011**, *17*, 598.
[4] M. Feyen, C. Weidenthaler, F. Schüth, A. H. Lu, *Chem. Mater.* **2010**, *22*, 2955.
[5] A. H. Lu, W. C. Li, N. Matoussevitch, B. Spliethoff, H. Bönnemann, F. Schüth, *Chem. Commun.* **2005**, 98.
[6] J. C. Park, J. U. Bang, J. Lee, C. H. Ko, H. Song, *J. Mater. Chem.* **2010**, *20*, 1239.
[7] L. M. Liz-Marzán, M. Giersig, P. Mulvaney, *Langmuir* **1996**, *12*, 4329.
[8] M. Kim, K. Sohn, H. B. Na, T. Hyeon, *Nano Lett.* **2002**, *2*, 1383.
[9] J. Y. Kim, S. B. Yoon, J.-S. Yu, *Chem. Commun.* **2003**, 790.
[10] Y. H. Ng, S. Ikeda, T. Harada, S. Higashida, T. Sakata, H. Mori, M. Matsumura, *Adv. Mater.* **2007**, *19*, 597.
[11] S. Ikeda, S. Ishino, T. Harada, N. Okamoto, T. Sakata, H. Mori, S. Kuwabata, T. Torimoto, M. Matsumura, *Angew. Chem. Int. Ed.* **2006**, *45*, 7063.
[12] T. Harada, S. Ikeda, Y. H. Ng, T. Sakata, H. Mori, T. Torimoto, M. Matsumura, *Adv. Funct. Mater.* **2008**, *18*, 2190.
[13] E. V. Shevchenko, M. I. Bodnarchuk, M. V. Kovalenko, D. V. Talapin, R. K. Smith, S. Aloni, W. Heiss, A. P. Alivisatos, *Adv. Mater.* **2008**, *20*, 4323.
[14] H. G. Yang, H. C. Zeng, *J. Phys. Chem. B* **2004**, *108*, 3492.
[15] J. Li, H. C. Zeng, *Angew. Chem. Int. Ed.* **2005**, *44*, 4342.
[16] W. S. Choi, H. Y. Koo, D. Y. Kim, *Langmuir* **2008**, *24*, 4633.
[17] D. K. Yi, S. S. Lee, G. C. Papaefthymiou, J. Y. Ying, *Chem. Mater.* **2006**, *18*, 614.
[18] A. B. Fuertes, M. Sevilla, T. Valdes-Solis, P. Tartaj, *Chem. Mater.* **2007**, *19*, 5418.
[19] H. Li, C.-S. Ha, I. Kim, *Macromol. Rapid Commun.* **2009**, *30*, 188.
[20] H. J. Hah, J. I. Um, S. H. Han, S. M. Koo, *Chem. Commun.* **2004**, 1012.
[21] R. Güttel, M. Paul, C. Galeano, F. Schüth, *J. Catal.* **2012**, *289*, 100.
[22] R. Güttel, M. Paul, F. Schüth, *Chem. Commun.* **2010**, *46*, 895.
[23] R. Güttel, M. Paul, F. Schüth, *Catal. Sci. Technol.* **2011**, *1*, 65.
[24] I. Lee, J. B. Joo, Y. Yin, F. Zaera, *Angew. Chem. Int. Ed.* **2011**, *50*, 10208.
[25] S. Zhang, X.-Z. Yuan, J. N. C. Hin, H. Wang, K. A. Friedrich, M. Schulze, *J. Power Sources* **2009**, *194*, 588.
[26] J. C. Meier, C. Galeano, I. Katsounaros, A. A. Topalov, A. Kostka, F. Schüth, K. J. J. Mayrhofer, *ACS Catalysis* **2012**, *2*, 832.
[27] J. C. Meier, I. Katsounaros, C. Galeano, H. Bongard, A. A. Topalov, A. Kostka, A. Karschin, F. Schüth, K. J. J. Mayrhofer, *Energy Environ. Sci.* **2012**, *5*, 9319.
[28] R. Borup, J. Meyers, B. Pivovar, Y. S. Kim, R. Mukundan, N. Garland, D. Myers, M. Wilson, F. Garzon, D. Wood, P. Zelenay, K. More, K. Stroh, T. Zawodzinski, J. Boncella, J. E. McGrath, M. Inaba, K. Miyatake, M. Hori, K. Ota, Z. Ogumi, S. Miyata, A. Nishikata, Z. Siroma, Y. Uchimoto, K. Yasuda, K.-I. Imijima, N. Iwashita, *Chem. Rev.* **2007**, *107*, 3904.
[29] Y. Shao-Horn, W. C. Sheng, S. Chen, P. J. Ferreira, E. F. Holby, D. Morgan, *Top. Catal.* **2007**, *46*, 285.
[30] C. Galeano, J. Meier, V. Peinecke, H. J. Bongard, I. Katsounaros, A. Topalov, A. H. Lu, K. J. J. Mayrhofer, F. Schüth, *J. Am. Chem. Soc.* **2012**, *134*, 20457.
[31] C. Galeano, R. Güttel, P. Michael, P. Arnal, A. H. Lu, F. Schüth, *Chem. Eur. J.* **2012**, *17*, 8434.
[32] C. Graf, D. L. J. Vossen, A. Imhof, A. van Blaaderen, *Langmuir* **2003**, *19*, 6693.
[33] G. Büchel, K. K. Unger, A. Matsumoto, K. Tsutsumi, *Adv. Mater.* **1998**, *10*, 1036.
[34] L. Qian, Y. Sha, X. Yang, *Thin Solid Films* **2006**, *515*, 1349.
[35] C. Weidenthaler, *Nanoscale* **2011**, *3*, 792.
[36] D. Mott, J. Luo, P. N. Njoki, Y. Lin, L. Wang, C. J. Zhong, *Catal. Today* **2007**, *122*, 378.
[37] J. Luo, M. M. Maye, V. Petkov, N. N. Kariuki, L. Wang, P. Njoki, D. Mott, Y. Lin, C.-J. Zhong, *Chem. Mater.* **2005**, *17*, 3086.

© 2013 WILEY-VCH Verlag GmbH & Co. KGaA, Weinheim

[38] D. Mott, J. Luo, A. Smith, P. Njoki, I. Wang, C.-J. Zhong, *Nanoscale Res. Lett.* **2006**, *2*, 12.
[39] B. N. Wanjala, J. Luo, R. Loukrakpam, B. Fang, D. Mott, P. N. Njoki, M. Engelhard, H. R. Naslund, J. K. Wu, L. Wang, O. Malis, C.-J. Zhong, *Chem. Mater.* **2010**, *22*, 4282.
[40] S. Xiao, W. Hu, W. Luo, Y. Wu, X. Li, H. Deng, *Eur. Phys. J. B* **2006**, *54*, 479.
[41] B. Fang, B. N. Wanjala, X. Hu, J. Last, R. Loukrakpam, J. Yin, J. Luo, C.-J. Zhong, *J. Power Sources* **2011**, *196*, 659.
[42] K. Hartl, K. J. J. Mayrhofer, M. Lopez, D. Goia, M. Arenz, *Electrochem. Commun.* **2010**, *12*, 1487.
[43] X. Li, J. Liu, W. He, Q. Huang, H. Yang, *J. Coll. Interf. Sci.* **2010**, *344*, 132.
[44] J. Luo, P. N. Njoki, Y. Lin, L. Wang, C.-J. Zhong, *Electrochem. Commun.* **2006**, *8*, 581.
[45] W. Tang, S. Jayaraman, T. F. Jaramillo, G. D. Stucky, E. W. McFarland, *J. Phys. Chem. C* **2009**, *113*, 5014.
[46] H. Ataee-Esfahani, L. Wang, Y. Nemoto, Y. Yamauchi, *Chem. Mater.* **2010**, *22*, 6310.
[47] Y. Lou, M. M. Maye, L. Han, J. Luo, C.-J. Zhong, *Chem. Commun.* **2001**, 473.
[48] J. Luo, M. M. Maye, N. N. Kariuki, L. Wang, P. Njoki, Y. Lin, M. Schadt, H. R. Naslund, C.-J. Zhong, *Catal. Today* **2005**, *99*, 291.
[49] J. Luo, P. N. Njoki, Y. Lin, D. Mott, P. Wang, C.-J. Zhong, *Langmuir* **2006**, *22*, 2892.
[50] Y. Xu, Y. Dong, J. Shi, M. Xu, Z. Zhang, X. Yang, *Catal. Commun.* **2011**, *13*, 54.
[51] A. A. Topalov, I. Katsounaros, J. C. Meier, S. O. Klemm, K. J. J. Mayrhofer, *Rev. Sci. Instr.* **2011**, *82*, 114103.
[52] K. J. J. Mayrhofer, M. Arenz, B. B. Blizanac, V. Stamenkovic, P. N. Ross, N. M. Markovic, *Electrochim. Acta* **2005**, *50*, 5144.

© 2013 WILEY-VCH Verlag GmbH & Co. KGaA, Weinheim